



1 **The impact threshold of the aerosol radiation forcing on the boundary layer**  
2 **structure in the pollution region**

3 Dandan Zhao<sup>†1,2</sup>; Jinyuan Xin<sup>\*†1,2</sup>; Chongshui Gong<sup>3</sup>; Jiannong Quan<sup>4</sup>; Yuesi Wang<sup>1,2</sup>; Guiqian  
4 Tang<sup>1</sup>, Yongxiang Ma<sup>1</sup>, Lindong Dai<sup>1</sup>, Xiaoyan Wu<sup>1</sup>, Guangjing Liu<sup>1</sup>, Yongjing Ma<sup>1</sup>

5 1 State Key Laboratory of Atmospheric Boundary Layer Physics and Atmospheric Chemistry (LAPC), Institute of  
6 Atmospheric Physics, Chinese Academy of Sciences, Beijing 100029, China

7 2 University of Chinese Academy of Sciences, Beijing 100049, China

8 3 Institute of Arid Meteorology, China Meteorological Administration, Lanzhou 730020, China

9 4 Institute of Urban Meteorology, Chinese Meteorological Administration, Beijing, China

10 (†) These authors contributed equally to this study.

11 (\*) Correspondence: Jinyuan Xin; email: [xjy@mail.iap.ac.cn](mailto:xjy@mail.iap.ac.cn); phone: (+86)15810006545; address: #40 Huayanli,  
12 Chaoyang District, Beijing 100029, China

13 **Abstract:** Recently, there has been increasing interest in the relation between  
14 particulate matter (PM) pollution and atmospheric boundary layer (ABL) structure.  
15 However, this has yet to be fully understood because most studies have been superficial.  
16 This study aimed to qualitatively assess the interaction between PM and ABL structure  
17 in essence, and to further quantitatively estimate the effects of aerosol radiative forcing  
18 (ARF) on the ABL structure. Multi-episode contrastive analysis stated the key to  
19 determining whether haze outbreak or dissipation was the ABL structure (i.e., stability  
20 and turbulence kinetic energy (TKE)) satisfied relevant conditions. However, it seemed  
21 that the ABL structure change was in turn highly related to the PM level and ARF. |SFC-  
22 ATM| (SFC and ATM is respectively the ARF at the surface and interior of the  
23 atmospheric column) is the absolute difference between ground and atmosphere layer  
24 ARFs, and the change in |SFC-ATM| is linearly related to the PM mass concentration.  
25 However, the influence of ARF on the boundary layer structure is nonlinear. With  
26 increasing |SFC-ATM|, the TKE level exponentially decreased, which was notable in  
27 the lower layers/ABL but disappeared above the ABL. Moreover, the threshold of the  
28 ARF effects on the ABL structure was determined for the first time, namely, once |SFC-  
29 ATM| exceeded  $\sim 55 \text{ W m}^{-2}$ , the ABL structure would quickly stabilize and would



30 thereafter change little with increasing ARF. The threshold of the ARF effects on the  
31 boundary layer structure could provide useful information for relevant atmospheric  
32 environment improvement measures and policies, such as formulating the objectives of  
33 phased air pollution control.

34 **Keywords:** boundary layer structure; aerosol radiative forcing; threshold; haze  
35 pollution

### 36 **1 Introduction**

37 Most areas in China, such as the North China Plain (Li et al., 2020; Xu et al., 2019),  
38 have suffered from a poor air quality as a result of the rapid economic growth. Beijing,  
39 as the Chinese capital and major city in the North China Plain, has frequently  
40 experienced severe and persistent haze events, characterized by an exceedingly high  
41 particulate matter (PM) mass loading suspended in near-surface air (Wang et al., 2018;  
42 Zhong et al., 2018). As previous studies have found, air pollution episodes are the result  
43 of secondary aerosol formation and adverse meteorological conditions (An et al., 2019;  
44 Guo et al., 2014; Li et al., 2017; Wang et al., 2014; Zheng et al., 2015; Wang et al.,  
45 2012). PM is concentrated in the atmospheric boundary layer (ABL) (Petaja et al., 2016;  
46 Tie et al., 2017), which is the lower part of the troposphere and is directly affected by  
47 the surface (Quan et al., 2013). The diffusion, transmission, and accumulation of  
48 pollutants are closely linked to ABL structure (meteorological conditions) variation  
49 (Han et al., 2009; Kotthaus and Grimmond, 2018; Zheng et al., 2017). Numerous  
50 studies have revealed that the meteorological factors in the boundary layer influence  
51 the formation of air pollution periods (Hua et al., 2016; Liu et al., 2016; Miao et al.,  
52 2018; Wang et al., 2012; Wang et al., 2014; Zhang et al., 2018). For instance, the  
53 aerosols concentrated in the ABL exhibit a strong negative relationship with the ABL  
54 height (ABLH) that determines the volume available for pollutant dispersion (Haman  
55 et al., 2014; Schaefer et al., 2009; Su et al., 2018; Tang et al., 2016). Heavy air pollution  
56 episodes have always occurred with persistent temperature inversions (Xu et al., 2019;  
57 Zhong et al., 2017). Weak/calm winds are important in the long-term increase in air  
58 pollutants (Niu et al., 2010; Yang et al., 2016). Additionally, previous studies have



59 reported that severe air pollution is always highly related to a high atmospheric  
60 humidity, which is one of the manifestations of stagnant ABL conditions (Tie et al.,  
61 2017; Petaja et al., 2016). Moreover, the feedback/interaction mechanism between the  
62 boundary layer structure and aerosol loading during severe pollution events has been  
63 analyzed in previous studies (Huang et al., 2018; Liu et al., 2018; Zhong et al., 2018;  
64 Zhao et al., 2019).

65 However, most of the work was performed through relationship analysis of the PM  
66 concentration and meteorological factors and only considered certain pollution  
67 processes. Few attempts have been made to examine the interaction between the ABL  
68 and air pollution in terms of essential aspects. Since the ABL is directly influenced by  
69 the surface, it is the only atmosphere layer characterized by turbulent activities, while  
70 higher atmosphere layers are weakly turbulent because of the strongly stable  
71 stratification (Munro, 2005). Thus, the ABL acts as a notable turbulence buffer coupling  
72 the surface with the free atmosphere, and PM and gas pollutants are only suspended in  
73 the ABL and are convectively spread throughout it. The evolution of the ABL structure,  
74 which plays a key role in pollutant accumulation/diffusion, is substantially the change  
75 in turbulent kinetic energy (TKE) in the ABL (Garratt et al., 1992). Therefore, we  
76 systematically analyzed the way the ABL interacts with pollutants via contrastive  
77 analysis of multiple haze episodes based on not only specific meteorological factors but  
78 also turbulent activity profiles and atmospheric stability indicators. Moreover, the  
79 change in solar radiation reaching the ground drives the diurnal ABL evolution  
80 considering the variation in atmospheric stability (Andrews, 2000). Since a strong  
81 aerosol radiative effect occurs on severe air pollution, the diurnal evolution of the  
82 atmospheric thermodynamic status is greatly affected (Dickerson et al., 1997; Stone et  
83 al., 2008; Wilcox et al., 2016). As previous studies have reported, the aerosol radiative  
84 forcing (ARF) is also a critical parameter that can further modify the boundary layer  
85 structure during haze episodes (Huang et al., 2018; Liu et al., 2018; Zhong et al., 2018).  
86 However, the influence degree of the aerosol radiative effect on the boundary layer  
87 structure remains unclear. Quantitatively determining the effects of ARF on the ABL



88 structure is urgently needed. Furthermore, this paper would analyze the interaction  
89 between the ABL structure and air pollution using high-resolution and real-observation  
90 datasets, such as temperature and humidity profiles of microwave radiometers,  
91 horizontal and vertical wind vector profiles of Doppler wind lidar, ABL heights (ABLH)  
92 and aerosol backscattering coefficient profiles of ceilometers. Wind profile lidar and  
93 microwave radiometers have the advantage of providing direct and continuous  
94 observations of the boundary layer over long periods of time and can characterize the  
95 ABL structure up to 2-3 km (Pichugina et al., 2019; Zhao et al., 2019), compensating  
96 for the deficiencies of previous research.

## 97 **2 Data and methods**

98 We conducted a two-month measurement campaign of the PM concentration and  
99 aerosol optical depth (AOD) and obtained vertical profiles of atmospheric parameters  
100 such as the temperature, humidity, wind vectors, atmospheric stability and TKE to  
101 better understand how the boundary layer structure responds to aerosol radiative effects.  
102 Figure S1 shows the observation site of the Tower Branch of the Institute of  
103 Atmospheric Physics (IAP), Chinese Academy of Sciences (39° 58' N, 116° 22' E;  
104 altitude: 58 m) and the sampling instruments in this study. The IAP site represents a  
105 typical urban Beijing site and all the sampling instruments are placed at the same  
106 location, and simultaneous monitoring is conducted. The algorithm of SBDART (Santa  
107 Barbara DISORT Atmospheric Radiative Transfer) (Levy et al., 2007) is the core model  
108 to calculate the radiative forcing parameters. Standard mid-latitude atmosphere is used  
109 in SBDART in Beijing. AOD and Angstrom Exponent (AE) at 550 nm were obtained  
110 from sun-photometer. Multiple sets of Single Scattering Albedo (SSA) and  
111 backscattering coefficient were calculated based on MIE theory and surface albedo &  
112 path radiation were read from MODIS (MOD04) which is used to calculate radiative  
113 forcing at top of atmosphere (TOA). The TOA results were combined with MODIS  
114 observations, the result which has the lowest deviation are defined as the actual  
115 parameters of aerosols and this set of parameters would be used to calculate the  
116 radiative forcing at the surface, top and interior of the atmospheric column (Gong et al.,



117 2014). Hourly radiative forcing parameters, including the ARF at the top (TOA),  
118 surface (SFC) and interior of the atmospheric column (ATM) at an observation site in  
119 Beijing can be calculated based on this algorithm. More detailed descriptions are  
120 provided in our previous work (Xin et al., 2016).

121 Air temperature and relative and absolute humidity profiles were retrieved with a  
122 microwave radiometer (hereinafter referred to as MWR) (RPG-HATPRO-G5 0030109,  
123 Germany). The MWR produces profiles with a resolution ranging from 10-30 m up to  
124 0.5 km, profiles with a resolution ranging from 40-70 m between 0.5 and 2.5 km and  
125 profiles with a resolution ranging from 100-200 m from 2 to 10 km at a temporal  
126 resolution of 1 s. More detailed information of the RPG-HATPRO-type instrument can  
127 be found at <http://www.radiometer-physics.de> (last access: 4 June 2020). Vertical wind  
128 speed and horizontal wind vector profiles were obtained by a 3D Doppler wind lidar  
129 (Windcube 100s, Leosphere, France). The wind measurement results have a spatial  
130 resolution ranging from 1-20 m up to 0.3 km and a spatial resolution of 25 m from 0.3  
131 to 3 km, at a temporal resolution of 1 s. More instrument details can be found at  
132 [www.leosphere.com](http://www.leosphere.com) (last access: 4 June 2020). A ceilometer (CL51, Vaisala, Finland)  
133 was adopted to acquire atmospheric backscattering coefficient (BSC) profiles. The  
134 CL51 ceilometer digitally receives the return backscattering signal from 0 to 100  $\mu$ s  
135 and provides BSC profiles with a spatial resolution of 10 m from the ground to a height  
136 of 15 km. The ABLH was further identified by the sharp change in the negative gradient  
137 of the BSC profile (Münkel et al., 2007) and a detailed information is reported in  
138 previous studies (Tang et al., 2015, 2016; Zhu et al., 2018). A CIMEL sun-photometer  
139 (CE318, France), a multichannel, automatic sun-and-sky scanning radiometer (Gregory  
140 2011), was used to observe the AOD, and the AOD at 500 nm is adopted in this paper.  
141 The real-time hourly mean ground levels of PM<sub>2.5</sub> (particulate matter with aerodynamic  
142 diameter less than or equal to 2.5  $\mu$ m) and PM<sub>10</sub> (particulate matter with aerodynamic  
143 diameter less than or equal to 10  $\mu$ m) were downloaded from the China National  
144 Environmental Monitoring Center (CNEMC) (available at  
145 <http://106.37.208.233:20035/>, last access: 4 June 2020).



146 The virtual potential temperature ( $\theta_v$ ) and pseudoequivalent potential temperature  
147 ( $\theta_{se}$ ) are calculated with Eqs. (1) and (2), respectively:

$$148 \quad \theta_v = T(1 + 0.608q)\left(\frac{1000}{p}\right)^{0.286} \quad (1)$$

$$149 \quad \theta_{se} = T\left(\frac{1000}{p}\right)^{0.286} \exp\left(\frac{r_s L_v}{C_{pd} T}\right) \quad (2)$$

150 where  $T$  is the air temperature,  $q$  is the specific humidity,  $p$  is the air pressure,  $r_s$  is the  
151 saturation mixing ratio,  $L_v$  is the latent heat of vaporization at  $2.5 \times 10^6$  J kg<sup>-1</sup> and  $C_{pd}$   
152 is the specific heat of air at 1005 J kg<sup>-1</sup> K<sup>-1</sup>. All the relevant parameters can be calculated  
153 from the temperature and humidity profile data obtained with the MWR, and the values  
154 of  $\theta_v$  and  $\theta_{se}$  at different altitudes can be then further obtained. The hourly TKE is  
155 calculated as:

$$156 \quad \text{TKE} = 0.5 \times (\delta_u^2 + \delta_v^2 + \delta_w^2). \quad (3)$$

157 The one-hour vertical velocity standard deviation ( $\delta_w^2$ ) and one-hour horizontal wind  
158 standard deviation ( $\delta_u^2$ ;  $\delta_v^2$ ) are calculated with Eqs. (4), (5) and (6), respectively:

$$159 \quad \delta_w^2 = \frac{1}{N-1} \sum_{i=1}^N (w_i - \bar{w})^2 \quad (4)$$

$$160 \quad \delta_u^2 = \frac{1}{N-1} \sum_{i=1}^N (u_i - \bar{u})^2 \quad (5)$$

$$161 \quad \delta_v^2 = \frac{1}{N-1} \sum_{i=1}^N (v_i - \bar{v})^2 \quad (6)$$

162 where  $N$  is the number of records per hour,  $w_i$  is the  $i$ th vertical wind velocity (m s<sup>-1</sup>),  
163  $u_i$  ( $v_i$ ) is the  $i$ th horizontal wind speed (m s<sup>-1</sup>),  $\bar{w}$  is the mean vertical wind speed (m  
164 s<sup>-1</sup>), and  $\bar{u}$  ( $\bar{v}$ ) is the mean horizontal wind speed (m s<sup>-1</sup>) (Banta et al., 2006; Wang et  
165 al., 2019).

### 166 **3 Results and discussion**

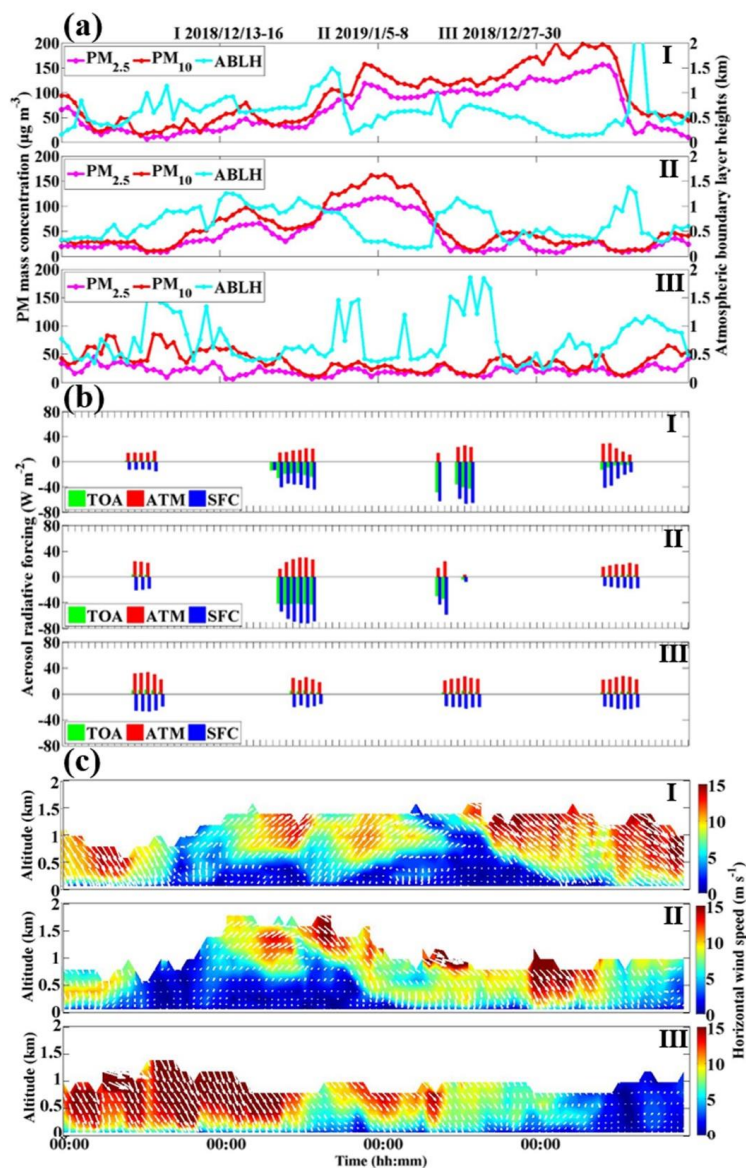
#### 167 **3.1 General haze episodes over Beijing in winter**

168 It is well known that severe air pollution episodes frequently occur in Beijing during  
169 autumn and winter (Jin-Xiang, 2007; Zhang et al., 2017). Two-month PM concentration  
170 data from Beijing in the winter of 2018 were collected. As expected, during this time,  
171 Beijing experienced severe and frequent haze pollution episodes with two heavy  
172 episodes in which the maximum hourly PM<sub>2.5</sub> concentration reached  $\sim 200$   $\mu\text{g m}^{-3}$  and six  
173 general episodes in which the PM<sub>2.5</sub> mass concentration ranged from  $\sim 100$ - $150$   $\mu\text{g m}^{-3}$



174 (Fig. S2(a)). Although the air pollution process is variable and complicated, it is worth  
175 stating that the haze pollution in Beijing in winter can be generally classified as two  
176 kinds of patterns, as shown in Fig. S2(b). For all haze episodes ①-⑦, the PM<sub>2.5</sub> mass  
177 concentration slowly increased in the afternoon of the first day, followed by a secondary  
178 maximum in the early morning and a maximum at midnight of the second day. In  
179 comparison to the processes of ④-⑦, where the PM<sub>2.5</sub> mass concentration sharply  
180 decreased to <25 μg m<sup>-3</sup> in the early morning of the third day, during periods ①-③,  
181 however, the highest PM<sub>2.5</sub> mass concentration (~100-200 μg m<sup>-3</sup>) was observed on the  
182 third day, which disappeared on the fourth day. As previously reported, transport,  
183 physical and chemical transformation and boundary layer structure (local  
184 meteorological conditions) are central to the determination of the amount and type of  
185 pollutant loading. The suspended particles in ④-⑦ were subjected to dispersal,  
186 controlled by the atmospheric motion (wind and turbulence) on the third day. The  
187 particles during periods ①-③ continued to accumulate and were therefore highly  
188 related to the specific ABL status. To investigate the possible reasons for the different  
189 variation trends of haze episodes ①-③ and ④-⑦, in the next section, we will mainly  
190 focus on the ABL structure (local meteorological conditions) considering transport and  
191 physical and chemical transformation.

192 **3.2 Qualitative analysis of the interaction between particulate matter and**  
193 **boundary layer structure**

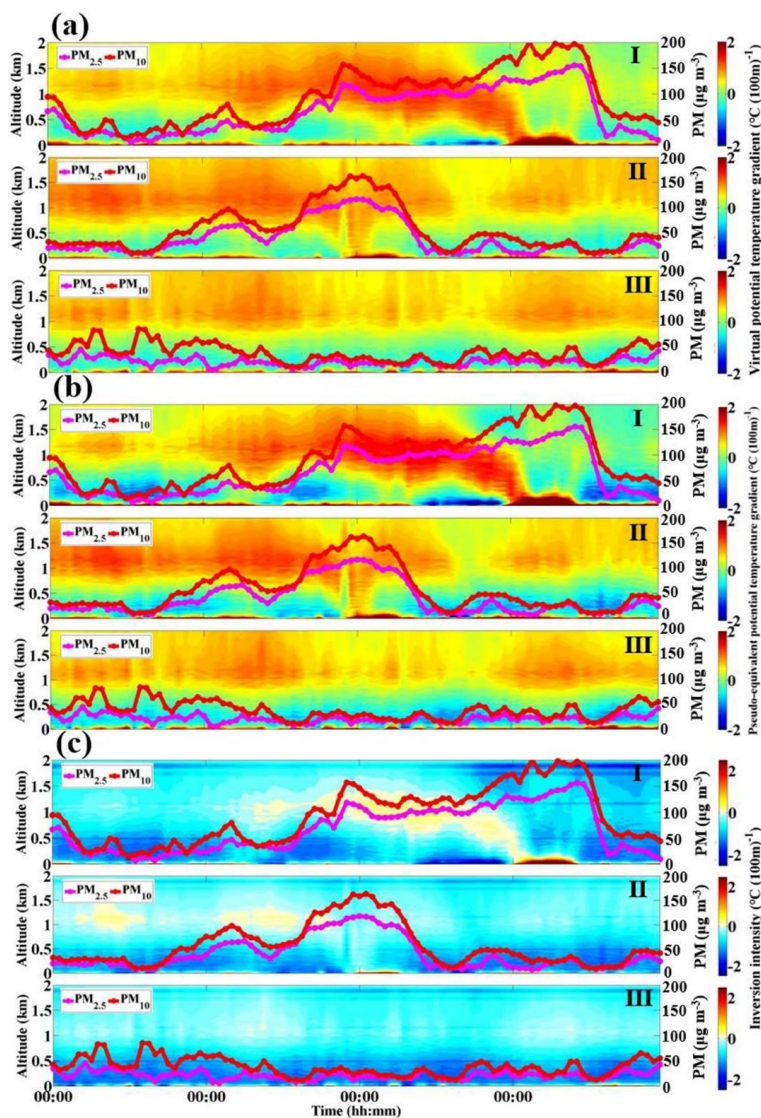


194

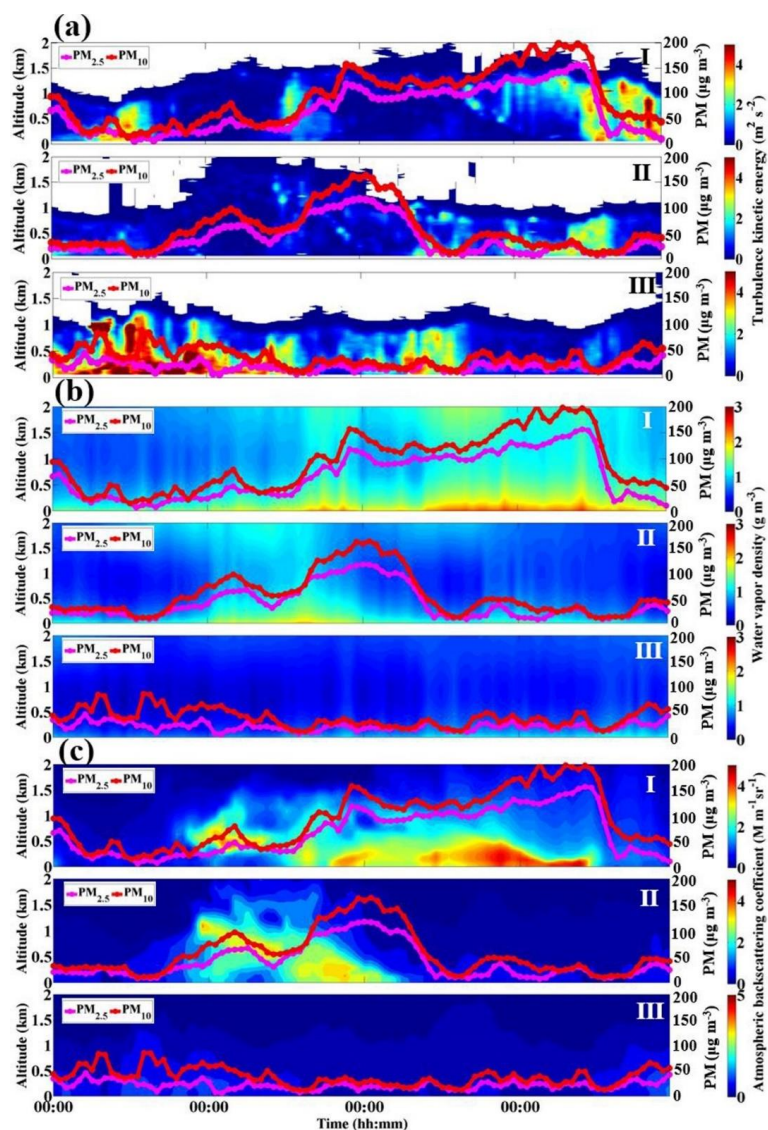
195 Figure 1. Temporal evolution of (a) the PM mass concentration and atmospheric  
196 boundary layer height (PM<sub>2.5</sub>: solid pink lines; PM<sub>10</sub>: solid red lines; ABLH: solid blue  
197 lines), (b) aerosol radiative forcing at the top (TOA; green bars), surface (SFC; blue  
198 bars) and interior of the atmospheric column (ATM; red bars), and (c) horizontal wind  
199 vector profiles (shaded colors: wind speeds; white arrows: wind vectors) during the



200 typical haze pollution episodes of I (2018/12/13-16) and II (2019/1/5-8) as well as the  
201 typical clean period of III (2018/12/27-30).



202  
203 Figure 2. Temporal variation in the vertical profiles of (a) the virtual potential  
204 temperature gradient ( $\partial\theta_v/\partial z$ ), (b) pseudoequivalent potential temperature gradient  
205 ( $\partial\theta_{se}/\partial z$ ) and (c) temperature inversion phenomenon (shaded colors: inversion intensity)  
206 during the typical haze pollution episodes of I (2018/12/13-16) and II (2019/1/5-8) as  
207 well as the typical clean period of III (2018/12/27-30).



208

209 Figure 3. Temporal variation in the vertical profiles of (a) the turbulent activity (shaded  
210 colors: TKE), (b) atmospheric humidity (shaded colors: vapor density) and (c) vertical  
211 distribution of suspended particles (shaded colors: BSC) during the typical haze  
212 pollution episodes of I (2018/12/13-16) and II (2019/1/5-8) as well as the typical clean  
213 period of III (2018/12/27-30).

214 As described in the previous section, although not exactly the same, the haze episodes  
215 followed two different kinds of variation trends. The specific reason for this finding



216 will be systematically analyzed in this section. To better illustrate the two different haze  
217 pollution patterns, a typical clean period will be considered as a control. The typical air  
218 pollution episodes of I (2018/12/13-16) and II (2019/1/5-8) as well as the typical clean  
219 period of III (2018/12/27-30) are chosen as examples for analysis. Numerous studies  
220 have reported that the original explosive growth of PM is caused by pollution transport  
221 under southerly winds (Ma et al., 2017; Zhao et al., 2019; Zhong et al., 2018). In this  
222 study, the action of southerly winds on the air pollution in Beijing was presented more  
223 clearly as the distribution of the horizontal wind vectors extending to heights of 1-1.5  
224 km (equivalent to the entire ABL) was obtained by the Windcube 100s lidar (Fig. 1(c)).  
225 On the 1<sup>st</sup> day of episodes I and II, the atmosphere layer up to ~1 km in height was  
226 controlled by strong and clean north winds, exactly like clean period III. Clearly, no  
227 pollution transport occurred, and the PM and ARF levels were equivalent to those on a  
228 clean day (Figs. 1(a)-(b)). The atmospheric backscattering coefficients throughout the  
229 ABL during the three episodes only ranged from ~0-1.5 M m<sup>-1</sup>sr<sup>-1</sup> (Fig. 3(c)). From the  
230 evening of the 1<sup>st</sup> day to the forenoon of the 2<sup>nd</sup> day, strong southerly winds blew across  
231 Beijing during both episodes I and II, with the wind speed increasing with the height,  
232 reaching ~5-15 m s<sup>-1</sup> at an atmosphere of about 0.5-1.5 km. The ABL during clean  
233 episode III was still dominated by north winds. Sensitive to the change in wind direction  
234 from north to south, the PM mass concentration progressively increased from a fairly  
235 low level to ~50 µg m<sup>-3</sup>. Moreover, the BSCs sharply increased to ~3 Mm<sup>-1</sup>rd<sup>-1</sup> and was  
236 concentrated at altitudes from ~0.5-1 km, which further stressed the effects of southerly  
237 transport on the original growth of the PM mass concentration over Beijing. With winds  
238 originating from the wetter south, compared to the low humidity during clean episode  
239 III, the air humidity in Beijing during this time notably increased with the vapor density  
240 ranging from ~1.5-2 g m<sup>-3</sup> during both episodes I and II (Fig. 3(b)). During the  
241 remainder of the 2<sup>nd</sup> day, the PM mass concentration continued to increase with south  
242 winds blowing and reached its highest level at midnight with a PM<sub>2.5</sub>/PM<sub>10</sub> mass  
243 concentration of ~110/150 µg m<sup>-3</sup> during both episodes I and II. The highest BSC values  
244 mainly occurred from the ground to a height of 1 km at this time, implying that a portion



245 of the suspended particles was pushed down to the near-surface. Noteworthy,  
246 regardless of the wind field, the atmospheric stratification states during this rising phase  
247 changed more notably. Before southerly wind transport occurred, the evolution of the  
248 stability indicator ( $\partial\theta_v/\partial z$ ;  $\partial\theta_{se}/\partial z$ ) profiles during episodes I and II was analogous to that  
249 during episode III (Figs. 2(a)-(b)). The stratification states at the different heights (0-1  
250 km) were either unstable or neutral, with negative or zero  $\partial\theta_v/\partial z$  values, respectively,  
251 whereby no clear nor strong temperature inversion phenomenon occurred in the lower  
252 atmosphere layer (Fig. 2(c)). The corresponding ABLHs were the same (Fig. 1(a)).  
253 However, the atmospheric stratification from  $\sim 0.5$ -1 km during episode I and from 0-1  
254 km during episode II became quite stable during the PM increase period, with positive  
255 values of  $\partial\theta_{se}/\partial z$  and almost no turbulent activity (TKE:  $\sim 0 \text{ m}^2 \text{ s}^{-2}$ ) (Fig. 3(a)). In contrast  
256 to an increased ABLH during clean period III, the ABLHs during episodes I-II sharply  
257 decreased. Considering that aerosol scattering and absorbing radiation could modify the  
258 temperature stratification (Li et al., 2010; Zhong et al., 2018), the aerosol radiation  
259 effect is too weak at a low PM level to change the latter, which defines the atmospheric  
260 stability. With the elevated PM level due to southerly transport, ARF also increased,  
261 with SFC (ATM) reaching  $\sim 40$  ( $\sim 20$ )  $\text{W m}^{-2}$  and  $\sim 75$  ( $\sim 30$ )  $\text{W m}^{-2}$  during episodes I  
262 and II, respectively. Less radiation reaching the ground and more heating the  
263 atmosphere above the ground, and in comparison to clean episode III, the atmospheric  
264 stratification during episodes I and II was altered. Besides, TOA has an analogous  
265 variation trend with SFC, increasing from quite low values to  $\sim 20 \text{ W m}^{-2}$  and  $\sim 45 \text{ W}$   
266  $\text{m}^{-2}$  during episodes I and II, respectively. It further clarified the high scattering effect  
267 of aerosols with the elevated PM level. The suspended particles carried by southerly  
268 transport originally occurring at high altitudes were restrained from vertically spreading  
269 and gradually sank due to gravity and accumulated near the surface. This stable  
270 stratification has a certain impact on aggravating haze pollution.

271 It is salient to note that the haze evolution trends during episodes I and II were  
272 basically consistent so far, corresponding to a similar ABL structure. Nevertheless, the  
273 north winds ( $\sim 10$ - $15 \text{ m s}^{-1}$ ) during episode II, which only blew above the ABL ( $>1 \text{ km}$ )

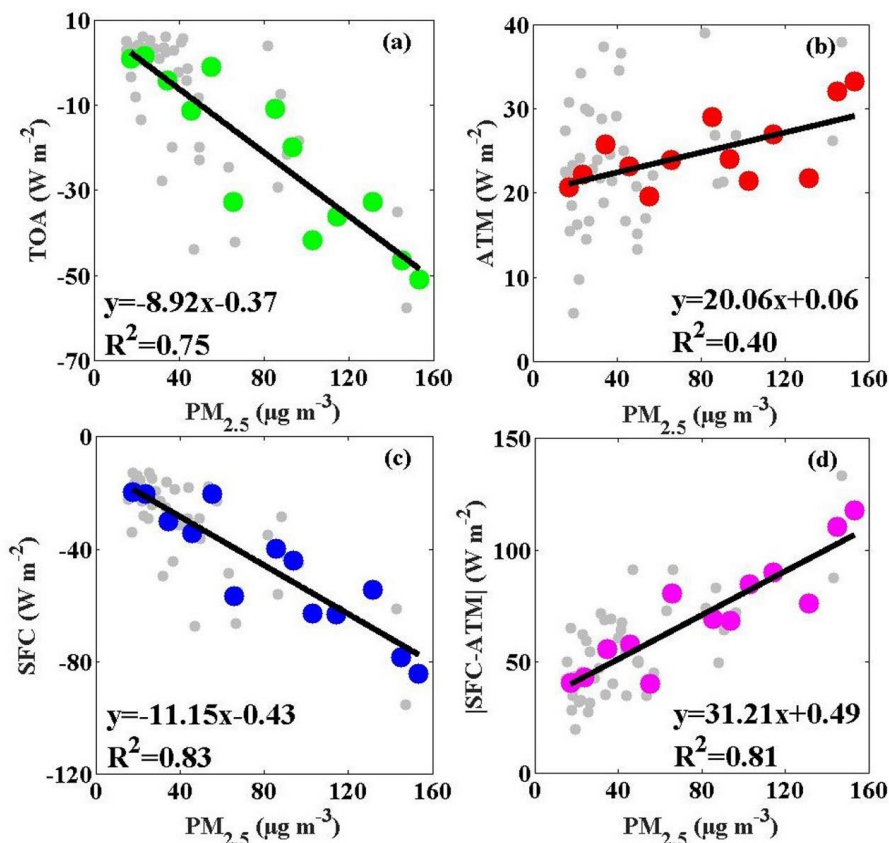


274 at midnight of the 2<sup>nd</sup> day, gradually spread downward and controlled the whole  
275 boundary layer on the 3<sup>rd</sup> day. Moreover, the south wind, which once was strong and  
276 filled the boundary layer on the 2<sup>nd</sup> day during episode I, gradually decelerated over  
277 time from the ground to high altitudes on the 3<sup>rd</sup> day. The wind field is critical with  
278 respect to horizontal dispersion in the boundary layer; thus, the strong, clean and dry  
279 north winds during episode II greatly diffused the already accumulated particles first,  
280 where the PM<sub>2.5</sub> mass concentration decreased from ~100 to ~50  $\mu\text{g m}^{-3}$ . The ARF  
281 decreased to the same level as that during clean period III, and with solar radiation  
282 heating the ground at noon on the 3<sup>rd</sup> day, the positive sensible heat flux (upward heat  
283 transfer) eliminated the previous night's temperature structure. The temperature  
284 stratification became similar to that on clean day III with a similar increase in ABLH.  
285 Thus, an unstable/neutral atmospheric state with a TKE of  $\sim 2 \text{ m}^2 \text{ s}^{-2}$  was also conducive  
286 to the vertical spread of materials, which were replaced with cleaner air from above. In  
287 response, the PM mass concentration (BSC) and air humidity during episode II  
288 gradually decreased and reached the same level as those during episode III. Conversely,  
289 the whole ABL (0-1 km) was controlled by calm/light winds during episode I on the 3<sup>rd</sup>  
290 day. On account of the calm/light winds, the horizontal wind shear sharply decreased,  
291 resulting in a decline in the intensity of mechanical turbulence. In the absence of an  
292 existing high PM mass concentration, strong ARF would continue to notably cool the  
293 ground and heat the aerosol layer, keeping the atmospheric stratification stable and thus  
294 decreasing the intensity of thermal turbulence. As can be seen in Fig. 1(b), SFC and  
295 TOA further increased up to  $\sim 40 \text{ W m}^{-2}$  and  $\sim 75 \text{ W m}^{-2}$ , respectively, with ATM  
296 remaining high ( $\sim 25 \text{ W m}^{-2}$ ). The ABLH barely changed on the 3<sup>rd</sup> day and maintained  
297 a lower altitude in the afternoon of the 4<sup>th</sup> day. Therefore, a rather stable atmosphere  
298 extended from  $\sim 0.3$ - $0.5 \text{ km}$  to  $\sim 1.5 \text{ km}$  on the 3<sup>rd</sup> day and from the ground to heights of  
299  $\sim 0.3 \text{ km}$  in the afternoon of the 4<sup>th</sup> day (Figs. 2(a)-(c)). The quite low TKE was highly  
300 consistent with the atmospheric stability stratification. Since the stable stratification  
301 acted as a lid at altitudes from  $0.5$ - $1.5 \text{ km}$ , downward momentum transport would be  
302 blocked, further explaining the calm/light winds in the lower atmosphere layer. In the



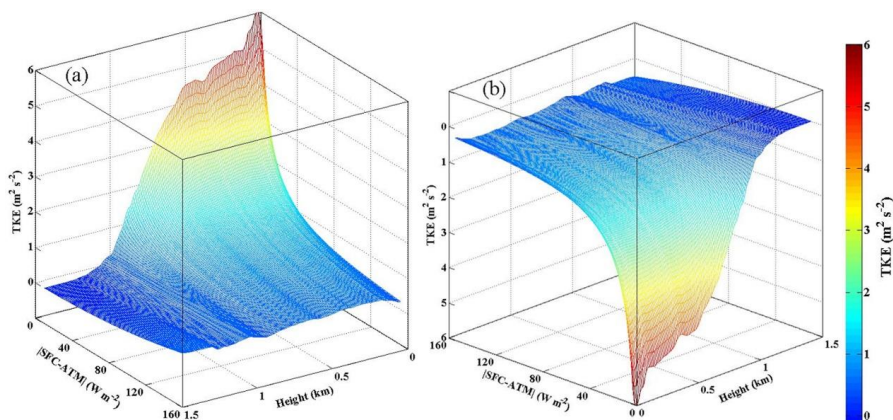
303 afternoon of the 4<sup>th</sup> day, it is worth noting that above the stable atmospheric stratification  
304 (0-0.3 km altitude), a relatively strong horizontal wind shear occurred corresponding to  
305 a TKE of  $\sim 1-2 \text{ m}^2 \text{ s}^{-2}$ . The accumulated particles near the surface were further inhibited  
306 right below the stable atmosphere layer, as reflected by the BSC distribution. This  
307 highlights the fact that a stable atmosphere with a weak turbulent activity was central  
308 to pushing down the pollutant layer. The same work was exerted on the water vapor as  
309 the air humidity at this time reached  $\sim 3 \text{ g m}^{-3}$  below an altitude of  $\sim 0.3 \text{ km}$ ,  
310 accompanied by intense heterogeneous hydrolysis reactions at the moist particle surface  
311 (Zhang et al., 2008), which further increased the PM mass concentration. In the  
312 afternoon of the 4<sup>th</sup> day, north winds spread down to the whole ABL, which promoted  
313 the horizontal and convective dispersion of pollutants and water vapor, and the PM  
314 mass concentration therefore dropped to the same level as that on clean day III. With  
315 quite low aerosol loading, the aerosol radiative effect was also quite weak and the ARF  
316 dropped to dropped to the level of that on clean day III. In this section, through a  
317 detailed contrastive analysis, we examined the potential reasons for the occurrence of  
318 the two different patterns of haze pollution and found that the crucial point in  
319 determining whether the PM mass concentration remained high or sharply decreased  
320 was related to whether the boundary layer remained stable. The boundary layer stability  
321 was in turn notably linked to the PM mass concentration and aerosol radiative effect.

322 **3.3 Quantitative analysis of the effect of particulate matter on the boundary layer**  
323 **structure**



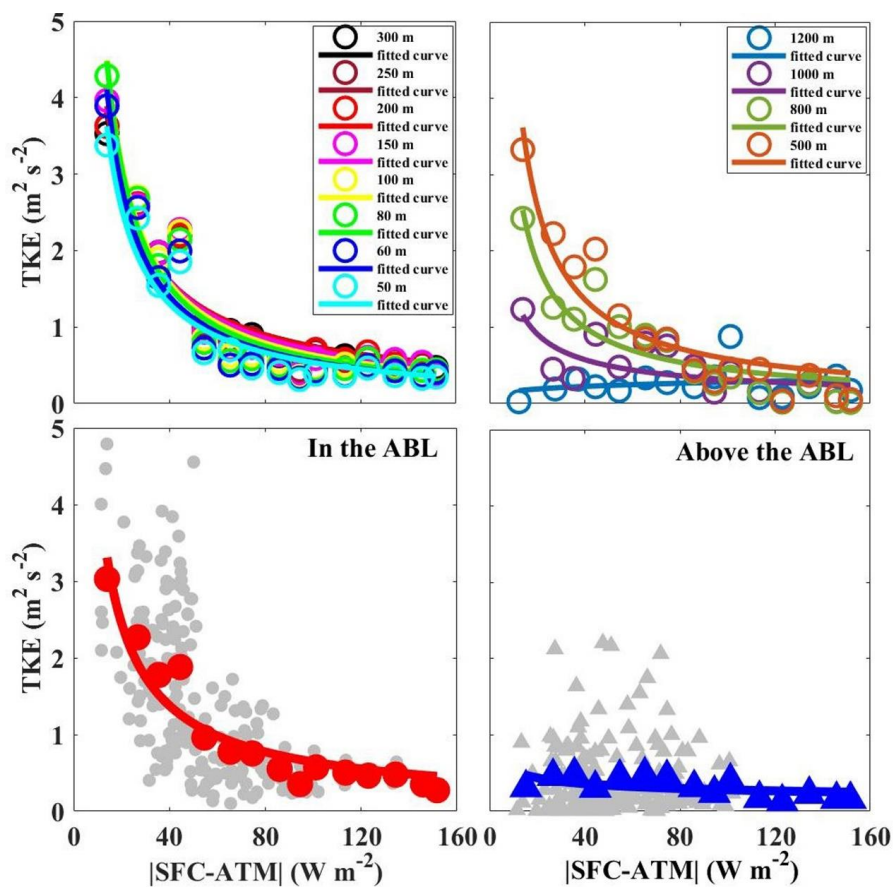
324

325 Figure 4. Scatter plots of the  $PM_{2.5}$  mass concentration (x) versus aerosol radiative  
326 forcing at the surface (SFC; y; a), interior of the atmospheric column (ATM; y; b) and  
327 top of the atmospheric column (TOA; y; c) as well as the absolute difference of SFC  
328 and ATM ( $|SFC-ATM|$ ; y; d), respectively (gray dots: daily data; other dots: mean data).  
329 The calculated daily data were collected over a two-month period in Beijing from 27  
330 November 2018 to 25 January 2019. (The daily data means daily mean values of TOA,  
331 ATM, SFC and corresponding daily averaged  $PM_{2.5}$  mass concentration. The mean  
332  $PM_{2.5}$  concentration were calculated at intervals of  $10 \mu g m^{-3}$  daily  $PM_{2.5}$  concentration,  
333 then the mean TOA, ATM and SFC were obtained after the average of the  
334 corresponding daily TOA, ATM and SFC, respectively.).

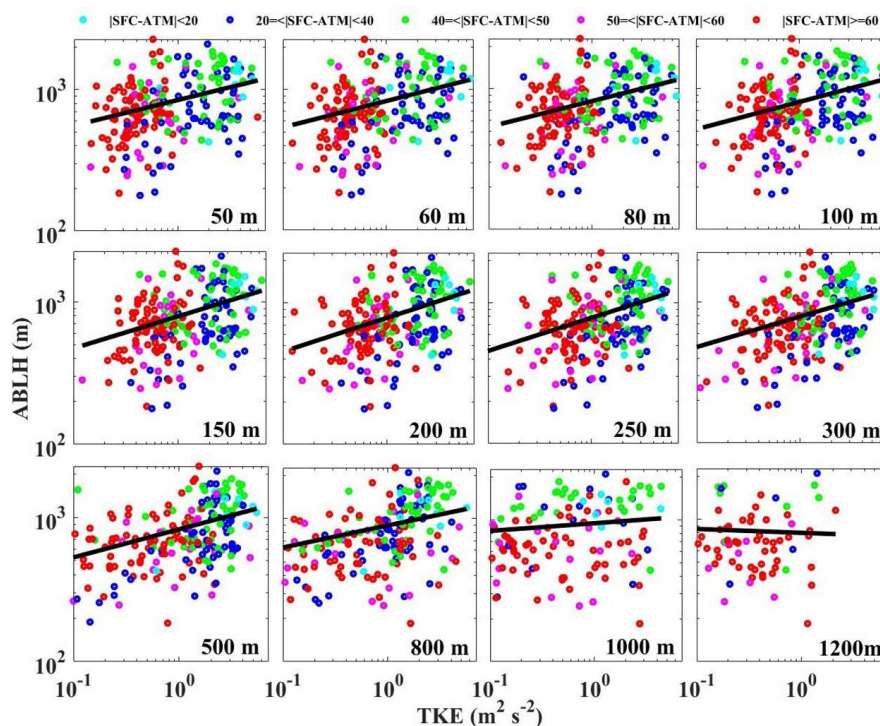


335

336 Figure 5. 3-D plot of the fitting relationship of the absolute difference in aerosol  
337 radiative forcing between the surface and interior of the atmospheric column ( $|SFC-$   
338  $ATM|$ ;  $x$ ) and turbulence kinetic energy (TKE;  $z$ ) at the different altitudes ( $y$ ) ((a) and  
339 (b) present different perspectives).



340  
341 Figure 6. Scatter plots of the mean absolute difference of the aerosol radiative forcing  
342 at the surface and interior of the atmospheric column ( $|SFC-ATM|$ ; x) versus the mean  
343 turbulence kinetic energy (TKE; y) at the different altitudes (the top row). Scatter plots  
344 of  $|SFC-ATM|$  (x) versus TKE (y) in the ABL and above the ABL (the bottom row;  
345 gray dots: hourly data; other dots: mean data). The hourly data were collected over a  
346 two-month period in Beijing from 27 November 2018 to 25 January 2019. (The hourly  
347 data means hourly mean values of  $|SFC-ATM|$  and corresponding hourly TKE. The  
348 mean  $|SFC-ATM|$  was averaged at intervals of  $10 \text{ W m}^{-2}$  hourly  $|SFC-ATM|$ , then the  
349 mean TKE was obtained after the average of the corresponding hourly TKE.).



350

351 Figure 7. The atmospheric boundary layer height (ABLH; y) as a function of the  
352 turbulence kinetic energy (TKE; x) at the different altitudes and the aerosol radiative  
353 effect defined as  $|SFC-ATM|$  (color code). The calculated hourly data used above are  
354 collected over a two-month period in Beijing from 27 November 2018 to 25 January  
355 2019.

356 Based on the contrastive analysis in the previous section, it was clear that the stable  
357 ABL structure played a critical role in the outbreak and maintenance of air pollution. It  
358 appeared that the increase in atmospheric stability suppressed pollution diffusion under  
359 a weak turbulence activity and low ABLH. Water vapor also greatly accumulated to a  
360 quite high level near the surface, further facilitating the formation of secondary aerosols.  
361 The evolution of ABL stability essentially occurred in response to the atmospheric  
362 temperature structure, as analyzed above, which was influenced by the strong aerosol  
363 radiation effect (Li et al., 2010; Andrews, 2000). The Archimedes buoyancy generated  
364 by the pulsating temperature field in the gravity field exerted negative work on the  
365 turbulent pulsating field with a stable ABL occurring, and the turbulence served as a



366 carrier for substance transport in the boundary layer, such as water vapor, heat and PM.  
367 (Garratt et al., 1992). Generally, the ABL structure controlling pollutant dissipation  
368 therefore greatly relies on the turbulent activity. Thus, in the following section, the ARF  
369 and TKE were chosen as the key parameters to examine how PM affects and modifies  
370 the boundary layer structure.

371 Figure 4 shows the relationship between the PM concentration and ARF. The  
372 aerosol scattering effect results in less radiation reaching the ground and the top of the  
373 atmospheric column, so the solar radiation levels reaching the ground and at the top of  
374 the atmospheric column differ with or without ambient aerosols, thus making SFC and  
375 TOA forcing. As shown in Figs. 4(a) and (c), SFC and TOA, respectively, were basically  
376 proportional to the  $PM_{2.5}$  concentration. With the increase in  $PM_{2.5}$  concentration, the  
377 solar radiation reaching the ground and at the top of the atmospheric column decreased,  
378 corresponding to a cooling of the ground and top of the atmospheric column. ATM,  
379 driven by aerosol absorption and representing a warming effect of aerosols on the  
380 atmosphere layer, exhibited a positive correlation with the  $PM_{2.5}$  concentration (see Fig.  
381 4(b)). These results demonstrated that a higher  $PM_{2.5}$  concentration would arouse a  
382 stronger ARF, further inhibiting solar radiation from reaching the ground, thus more  
383 notably heating the atmosphere layer.  $|SFC-ATM|$ , defined as the absolute value of the  
384 difference between SFC and ATM, represents the combined action of aerosols on the  
385 solar radiation reaching the aerosol layer and the ground. Larger values of  $|SFC-ATM|$   
386 indicate stronger aerosol scattering and/or absorption effects, further implying a more  
387 significant temperature difference between the ground and the above atmosphere layer.  
388 As expected, a positive linear correlation between  $|SFC-ATM|$  and  $PM_{2.5}$  concentration  
389 was found, as shown in Fig. 4(d).

390 As described in the above paragraph, there was a strong ARF under a high PM  
391 loading, which markedly altered the atmospheric temperature structure, further  
392 changing the ABL structure. It is necessary to determine the effect degree of ARF on  
393 the boundary layer structure. Figure 5 shows the 3-D plots of the fitting relationship  
394 between the hourly values of  $|SFC-ATM|$  and TKE at the different altitudes from



395 different perspectives. What stood out in Fig. 5(a) was the general decline in TKE with  
396 respect to the growth of |SFC-ATM|. With increasing |SFC-ATM| value, the TKE value  
397 at the different altitudes always decreased exponentially and approached zero below  
398  $\sim 0.8$  km. The notable exponential function between TKE and |SFC-ATM| explained  
399 that a strong ARF would drastically change the boundary layer into highly stable  
400 conditions characterized by a rather low TKE. The results above highlight the  
401 nonnegligible impact of the aerosol radiative effect on the boundary layer structure,  
402 especially during the haze episode under a high aerosol loading with a strong ARF. It is  
403 well known that a larger net negative/positive SFC/ATM means a cooler/warmer the  
404 ground/atmosphere would be. An increase in |SFC-ATM| implies the gradual  
405 intensification of the ground cooling and/or atmosphere heating processes. It therefore  
406 changed the atmospheric stratification into a gradually enhanced stable state, which was  
407 characterized by increasingly weaker turbulence activities. Additionally, as shown in  
408 Fig. 5(b), from another perspective, we can clearly identify a critical point of the |SFC-  
409 ATM| effects on TKE in the low layers. In particular, TKE decreased with increasing  
410 |SFC-ATM| and hardly changed when |SFC-ATM| exceeded the critical point. To define  
411 the critical point, we generated scatter plots of the average |SFC-ATM| and TKE at  
412 several altitudes, as shown in Figs. 6(a)-(b). The |SFC-ATM| had mean values of 10-20,  
413 20-30, ..., and 150-160  $\text{W m}^{-2}$ , and the corresponding mean TKE values were further  
414 calculated. The scatter plots of the unaveraged hourly data are shown in Fig. S3, and  
415 the fitting functions are listed in Table S1. Depending on the maximum curvature of the  
416 exponential curve (Silvanus and Gardner, 1998), a critical point should exist. With the  
417 mean TKE and |SFC-ATM| values on the exponential curve, we found that once the  
418 aerosol radiative effect defined by |SFC-ATM| exceeded 50-60  $\text{W m}^{-2}$  (average of  $\sim 55$   
419  $\text{W m}^{-2}$ ), the TKE sharply decreased from  $\sim 2 \text{ m}^2 \text{ s}^{-2}$  to lower than  $1 \text{ m}^2 \text{ s}^{-2}$ . This means  
420 that a high aerosol loading with a |SFC-ATM| value higher than  $\sim 55 \text{ W m}^{-2}$  would  
421 change the boundary layer from the unstable state to the extremely stable state in a short  
422 time, and further increasing |SFC-ATM| would barely modify the ABL structure. This  
423 result can provide useful information to explain why air pollution is sometimes



424 aggravated under a stable ABL and sometimes not. The average aerosol radiative  
425 forcing ( $|SFC-ATM|$ ) value of  $\sim 55 \text{ W m}^{-2}$  can be defined as the threshold of the ARF  
426 effects on the ABL structure, which could provide useful information for relevant model  
427 simulations, atmospheric environment improvement measures and relevant policies. In  
428 addition, as shown in Figs. 5 and 6, the exponential relationship between TKE and  
429  $|SFC-ATM|$  was notable in the low layers and gradually deteriorated with increasing  
430 altitude. On average, the exponential relationship was notable in the ABL and almost  
431 disappeared above the ABL (Figs. 6(c) and (d)). Considering that aerosols are mainly  
432 concentrated below the lower atmosphere, contributing the most to the SFC and ATM  
433 forcing, which further confirmed, the considerable change in atmospheric stratification  
434 caused by aerosols indeed existed and mainly occurred in the lower layers.

435 From the previous discussion, it is clear that a strong aerosol radiative effect  
436 markedly affected the turbulent activity and modified the boundary layer structure. As  
437 many studies have reported, the ABLH is an important meteorological factor that  
438 influences the vertical diffusion of atmospheric pollutants and water vapor (Stull, 1988;  
439 Robert and Aron, 1983). The following is an examination of the relationship among the  
440 turbulent activity, ARF and ABLH to illustrate the change in ABLH in response to ARF.  
441 Figure 7 shows the ABLH as a function of the TKE and  $|SFC-ATM|$  at the different  
442 altitudes. It was apparent from this figure that a positive correlation exists between TKE  
443 and ABLH. As the turbulent activity became increasingly weaker, the corresponding  
444 boundary layer height gradually decreased, which was in response to the gradual  
445 increase in  $|SFC-ATM|$ . Similar to the relationship between the turbulent activity and  
446 aerosol radiative effect, as shown in Fig. 6, the relationship among these aspects was  
447 much stronger below 300 m and almost disappeared above 800 m. This further  
448 addressed the fact that the change in boundary layer height was attributed to the  
449 turbulence activity variation, which stemmed from the aerosol radiative effect.

450 Thus far, this section has demonstrated that the aerosol loading with aerosol  
451 radiative effects impacted the turbulent activity, changed the boundary layer height and  
452 thus modified the boundary layer structure. On the other hand, it is now necessary to



453 explain how the renewed boundary layer structure modifies the  $PM_{2.5}$  concentration. As  
454 shown in Figs. S4(a)-(b), the ABLH as an independent variable has an impact on the  
455 ambient water vapor in the ABL at some degree. There was a steady increase in the  
456 ambient humidity with decreasing ABLH, where absolute humidity (AH) and relative  
457 humidity (RH) were projected to decrease to  $\sim 3 \text{ g m}^{-3}$  and  $\sim 60\%$ , respectively, with the  
458 ABLH decreasing below  $\sim 500 \text{ m}$ . With the increase in ambient humidity, a marked rise  
459 in  $PM_{2.5}$  concentration occurred, as shown in Figs. S4(c)-(d). Once AH and RH  
460 exceeded  $\sim 3 \text{ g m}^{-3}$  and  $\sim 60\%$ , respectively, the  $PM_{2.5}$  concentration reached  $\sim 100 \mu\text{g m}^{-3}$ .  
461 The results above indicate that with a fairly low boundary layer height, water vapor  
462 accumulated near the surface, and particles tended to hygroscopic growth, resulting in  
463 secondary aerosol formation in a high-humidity environment, further increasing the  
464  $PM_{2.5}$  concentration. As shown in Fig. S4(e), with the level off of the ABLH, the  $PM_{2.5}$   
465 mass concentration increased exponentially and reached a high value. The exponential  
466 relationship was similar to that between the ambient humidity and ABLH, which  
467 revealed that the explosive growth of the  $PM_{2.5}$  concentration under a low ABLH was  
468 largely driven by intense secondary aerosol formation and hygroscopic growth at a high  
469 ambient humidity.





485 satisfied relevant conditions. As previous studies reported (Huang et al., 2018; Liu et  
486 al., 2018; Zhong et al., 2018) and was confirmed in this paper, the extremely stable  
487 stratification with positive  $\partial\theta_{sc}/\partial z$  values and a low TKE was the premise of the outbreak  
488 of haze pollution. However, it appeared that the change/state of the boundary layer  
489 structure was in turn strongly linked to the PM mass concentration and ARF, and we  
490 further quantitatively evaluated the effect of ARF on the boundary layer structure. The  
491 Fig. 8 emerging from the foregoing observation analysis is one where ARF modifies  
492 the boundary layer structure and aggravates haze pollution. The aerosol effects on the  
493 atmospheric stratification depend on the reduced radiation reaching the ground due to  
494 aerosol scattering and absorbing radiation in the atmosphere (Dickerson et al., 1997;  
495 Stone et al., 2008; Wilcox et al., 2016). First, we found that there existed a positive  
496 linear relationship between |SFC-ATM| and  $PM_{2.5}$  concentration, which means that  
497 strong aerosol scattering and/or absorption effect occurred during the heavy haze  
498 episodes could arouse significant temperature differences between the ground and the  
499 above atmosphere layer. Previous studies revealed that black carbon solar absorption  
500 suppresses turbulence in the ABL (Wilcox et al., 2016), however, we found that the  
501 TKE value at the different altitudes always decreased exponentially and approached  
502 zero with increasing |SFC-ATM|, which was significant in the lower atmosphere layer  
503 and became gradually worse with increasing altitude. Then, we confirmed that the  
504 decrease in boundary layer height was attributed to the reduction in turbulence activity,  
505 stemming from the intensification of the aerosol radiative effect. Thus, with the increase  
506 in PM mass concentration, the temperature stratification at the different heights in the  
507 boundary layer gradually shifted from the normal state in which the turbulence activity  
508 is strong and the boundary layer height is quite high to the abnormal state that  
509 suppresses turbulence development and decreases the boundary layer height. The ARF  
510 effects on atmospheric stratification were more significant in the lower layer and  
511 disappeared above the boundary layer, which also confirmed that the stronger ARF  
512 from the aerosol layer would indeed change the boundary layer into the considerably  
513 stable state characterized by a rather low TKE. The change in ARF is linear due to the



514 PM concentration; however, the influence of ARF on the boundary layer structure is  
515 nonlinear. Based on the exponential relationship, the threshold of the ARF effects on  
516 the boundary layer structure has been determined for the first time in this paper, which  
517 highlighted that once the ARF exceeded a certain value, the boundary layer structure  
518 would quickly stabilize and thereafter changed little with increasing ARF. The  
519 discovery of this threshold further quantifies the feedback mechanism of the ARF on  
520 the boundary layer stability, and the occurrence of this feedback mechanism is directly  
521 related to the degree of pollution. The threshold of the ARF effects on the boundary  
522 layer stability can provide useful information for relevant atmospheric environment  
523 improvement measures and policies, such as formulating the objectives for phased air  
524 pollution control. When the  $PM_{2.5}$  concentration is controlled with the ARF below the  
525 threshold, the self-purification capacity of the atmosphere can effectively dilute and  
526 diffuse pollutants. The pollution concentration decreases rapidly, the weak ARF and  
527 free convection of the atmosphere produce a virtuous cycle, and the atmosphere  
528 maintains a high efficiency of self-purification. In contrast, when the  $PM_{2.5}$   
529 concentration increases with an ARF exceeding the threshold value, this further  
530 stabilizes the boundary layer, and the atmospheric environmental capacity rapidly  
531 decreases, especially near the stratum. The  $PM_{2.5}$  concentration further increases,  
532 aggravating haze pollution. In the process of air pollution control, there is a nonlinear  
533 relationship between the  $PM_{2.5}$  concentration in the atmosphere and the emission  
534 control amount of the source, which is also the most difficult stage for the control of  
535 polluted areas. On all accounts, this study provides the first comprehensive assessment  
536 of the interaction between PM and boundary layer structure through qualitative and  
537 quantitative analysis. The estimation of the ARF effects on the boundary layer structure  
538 can also be adopted as a reference in model studies.

#### 539 **Data availability**

540 The surface  $PM_{2.5}$  &  $PM_{10}$  and other trace gases observation data used in this study can  
541 be accessed from <http://106.37.208.233:20035/> (last access: 4 June 2020). Other  
542 datasets can be accessed upon request to the corresponding author.



543 **Author contribution**

544 ZD performed the research and wrote the paper. XJ provided writing guidance, revised  
545 and polished the paper. GC performed the SBDART model. QJ and WY GC contributed  
546 to discussions of results. TG and MY designed the experiments and DL, WX, LG and  
547 MY carried them out. All the authors have made substantial contributions to the work  
548 reported in the manuscript.

549 **Competing interests**

550 The authors declare that they have no conflict of interest.

551 **Acknowledgments**

552 This study was supported by the Ministry of Science and Technology of China  
553 (grant number 2016YFC0202001), the CAS Strategic Priority Research Program  
554 (XDA23020301) and the National Natural Science Foundation of China (grant number  
555 41375036). The authors are thankful for the data support from the National Earth  
556 System Science Data Sharing Infrastructure, National Science and Technology  
557 Infrastructure of China (available at <http://www.geodata.cn>, last access: 4 June 2020).

558 **References**

559 An, Z., Huang, R.-J., Zhang, R., Tie, X., Li, G., Cao, J., Zhou, W., Shi, Z., Han, Y., Gu, Z., and Ji,  
560 Y.: Severe haze in northern China: A synergy of anthropogenic emissions and atmospheric processes,  
561 *Proc. Natl. Acad. Sci. U. S. A.*, 116, 8657-8666, <https://doi.org/10.1073/pnas.1900125116>, 2019.

562 Andrews, D. G.: *An Introduction to Atmospheric Physics*, Cambridge University Press, 2000.

563 Banta, R. M., Pichugina, Y. L., and Brewer, W. A.: Turbulent velocity-variance profiles in the stable  
564 boundary layer generated by a nocturnal low-level jet, *J. Atmos. Sci.*, 63, 2700-2719,  
565 <https://doi.org/10.1175/jas3776.1>, 2006.

566 Dickerson, R. R., Kondragunta, S., Stenchikov, G., Civerolo, K. L., Doddridge, B. G., and Holben,  
567 B. N.: The impact of aerosols on solar ultraviolet radiation and photochemical smog, *Science* (New  
568 York, N.Y.), 278, 827-830, <https://doi.org/10.1126/science.278.5339.827>, 1997.

569 Garratt, J. R., Dessler, A. J., Houghton, J. T., and Rycroft, M. J.: The atmospheric boundary layer,  
570 1992.

571 Gong, C., Xin, J., Wang, S., Wang, Y., Wang, P., Wang, L., and Li, P.: The aerosol direct radiative



572 forcing over the Beijing metropolitan area from 2004 to 2011, *J. Aerosol Sci.*, 69, 62-70,  
573 <https://doi.org/10.1016/j.jaerosci.2013.12.007>, 2014.

574 Gregory, L.: Cimel Sunphotometer (CSPHOT) Handbook, 2011.

575 Guo, S., Hu, M., Zamora, M. L., Peng, J., Shang, D., Zheng, J., Du, Z., Wu, Z., Shao, M., Zeng, L.,  
576 Molina, M. J., and Zhang, R.: Elucidating severe urban haze formation in China, *Proc. Natl. Acad.*  
577 *Sci. U. S. A.*, 111, 17373-17378, <https://doi.org/10.1073/pnas.1419604111>, 2014.

578 Haman, C. L., Couzo, E., Flynn, J. H., Vizuete, W., Heffron, B., and Lefer, B. L.: Relationship  
579 between boundary layer heights and growth rates with ground-level ozone in Houston, Texas, *J.*  
580 *Geophys. Res.: Atmos.*, 119, 6230-6245, <https://doi.org/10.1002/2013jd020473>, 2014.

581 Han, S., Bian, H., Tie, X., Xie, Y., Sun, M., and Liu, A.: Impact of nocturnal planetary boundary  
582 layer on urban air pollutants: Measurements from a 250-m tower over Tianjin, China, *J. Hazard.*  
583 *Mater.*, 162, 264-269, <https://doi.org/10.1016/j.jhazmat.2008.05.056>, 2009.

584 Hua, Y., Wang, S., Wang, J., Jiang, J., Zhang, T., Song, Y., Kang, L., Zhou, W., Cai, R., Wu, D., Fan,  
585 S., Wang, T., Tang, X., Wei, Q., Sun, F., and Xiao, Z.: Investigating the impact of regional transport  
586 on PM<sub>2.5</sub> formation using vertical observation during APEC 2014 Summit in Beijing, *Atmos. Chem.*  
587 *Phys.*, 16, 15451-15460, <https://doi.org/10.5194/acp-16-15451-2016>, 2016.

588 Huang, X., Wang, Z., and Ding, A.: Impact of Aerosol-PBL Interaction on Haze Pollution: Multiyear  
589 Observational Evidences in North China, *Geophys. Res. Lett.*, 45, 8596-8603,  
590 <https://doi.org/10.1029/2018gl079239>, 2018.

591 Jin-Xiang, L. I.: The Characteristics and Cause Analysis of Heavy-Air-Pollution in Autumn and  
592 Winter in Beijing, *Environ. Monit. China*, 2007.

593 Kotthaus, S., and Grimmond, C. S. B.: Atmospheric boundary-layer characteristics from ceilometer  
594 measurements. Part 1: A new method to track mixed layer height and classify clouds, *Q. J. R.*  
595 *Meteorol. Soc.*, 144, 1525-1538, <https://doi.org/10.1002/qj.3299>, 2018.

596 Levy, R. C., Remer, L. A., and Dubovik, O.: Global aerosol optical properties and application to  
597 Moderate Resolution Imaging Spectroradiometer aerosol retrieval over land, *J. Geophys. Res.: Atmos.*,  
598 112, <https://doi.org/10.1029/2006jd007815>, 2007.

599 Li, G., Bei, N., Cao, J., Huang, R., Wu, J., Feng, T., Wang, Y., Liu, S., Zhang, Q., Tie, X., and Molina,  
600 L. T.: A possible pathway for rapid growth of sulfate during haze days in China, *Atmos. Chem. Phys.*,



- 601 17, 3301-3316, <https://doi.org/10.5194/acp-17-3301-2017>, 2017.
- 602 Li, M., Wang, L., Liu, J., Gao, W., Song, T., Sun, Y., Li, L., Li, X., Wang, Y., Liu, L., Daellenbach,  
603 K. R., Paasonen, P. J., Kerminen, V.-M., Kulmala, M., and Wang, Y.: Exploring the regional  
604 pollution characteristics and meteorological formation mechanism of PM<sub>2.5</sub> in North China during  
605 2013-2017, *Environ. Int.*, 134, <https://doi.org/10.1016/j.envint.2019.105283>, 2020.
- 606 Li, Z., Lee, K.-H., Wang, Y., Xin, J., and Hao, W.-M.: First observation-based estimates of cloud-  
607 free aerosol radiative forcing across China, *J. Geophys. Res.: Atmos.*, 115,  
608 <https://doi.org/10.1029/2009jd013306>, 2010.
- 609 Liu, Q., Jia, X., Quan, J., Li, J., Li, X., Wu, Y., Chen, D., Wang, Z., and Liu, Y.: New positive  
610 feedback mechanism between boundary layer meteorology and secondary aerosol formation during  
611 severe haze events, *Sci Rep*, 8, <https://doi.org/10.1038/s41598-018-24366-3>, 2018.
- 612 Liu, T. T., Gong, S., Meng, Y., Qi, C. Z., and Hong, L. L.: Contributions of meteorology and  
613 emission to the 2015 winter severe haze pollution episodes in Northern China, *Atmos. Chem. Phys.*,  
614 17, 1-17, <https://doi.org/10.5194/acp-2016-204>, 2016.
- 615 Münkel, C., Eresmaa, N., Rasanen, J., and Karppinen, A.: Retrieval of mixing height and dust  
616 concentration with lidar ceilometer, *Bound-Lay Meteorol*, 124, 117-128, <https://doi.org/10.1007/s10546-006-9103-3>, 2007.
- 618 Ma, Q., Wu, Y., Zhang, D., Wang, X., and Zhang, R.: Roles of regional transport and heterogeneous  
619 reactions in the PM<sub>2.5</sub> increase during winter haze episodes in Beijing, *Sci. Total Environ.*, 599-  
620 600, 246-253, <https://doi.org/10.1016/j.scitotenv.2017.04.193>, 2017.
- 621 Miao, Y., Guo, J., Liu, S., Zhao, C., Li, X., Zhang, G., Wei, W., and Ma, Y.: Impacts of synoptic  
622 condition and planetary boundary layer structure on the trans-boundary aerosol transport from  
623 Beijing-Tianjin-Hebei region to northeast China, *Atmos. Environ.*, 181, 1-11,  
624 <https://doi.org/10.1016/j.atmosenv.2018.03.005>, 2018.
- 625 Munro, D. S.: *Boundary Layer Climatology*, 2005.
- 626 Niu, F., Li, Z., Li, C., Lee, K.-H., and Wang, M.: Increase of wintertime fog in China: Potential  
627 impacts of weakening of the Eastern Asian monsoon circulation and increasing aerosol loading, *J.*  
628 *Geophys. Res.: Atmos.*, 115, <https://doi.org/10.1029/2009jd013484>, 2010.
- 629 Petaja, T., Jarvi, L., Kerminen, V. M., Ding, A. J., Sun, J. N., Nie, W., Kujansuu, J., Virkkula, A.,



- 630 Yang, X. Q., Fu, C. B., Zilitinkevich, S., and Kulmala, M.: Enhanced air pollution via aerosol-  
631 boundary layer feedback in China, *Sci Rep*, 6, <https://doi.org/10.1038/srep18998>, 2016.
- 632 Pichugina, Y. L., Banta, R. M., Bonin, T., Brewer, W. A., Choukulkar, A., McCarty, B. J., Baidar, S.,  
633 Draxl, C., Fernando, H. J. S., Kenyon, J., Krishnamurthy, R., Marquis, M., Olson, J., Sharp, J., and  
634 Stoelinga, M.: Spatial Variability of Winds and HRRR-NCEP Model Error Statistics at Three  
635 Doppler-Lidar Sites in the Wind-Energy Generation Region of the Columbia River Basin, *J. Appl.*  
636 *Meteorol. Climatol.*, 58, 1633-1656, <https://doi.org/10.1175/jamc-d-18-0244.1>, 2019.
- 637 Quan, J., Gao, Y., Zhang, Q., Tie, X., Cao, J., Han, S., Meng, J., Chen, P., and Zhao, D.: Evolution  
638 of planetary boundary layer under different weather conditions, and its impact on aerosol  
639 concentrations, *Particuology*, 11, 34-40, <https://doi.org/10.1016/j.partic.2012.04.005>, 2013.
- 640 Robert, and Aron: Mixing height—an inconsistent indicator of potential air pollution concentrations,  
641 *Atmos. Environ.*, 17, 2193-2197, [https://doi.org/10.1016/0004-6981\(83\)90215-9](https://doi.org/10.1016/0004-6981(83)90215-9), 1983.
- 642 Schaefer, K., Wang, Y., Muenkel, C., Emeis, S., Xin, J., Tang, G., Norra, S., Schleicher, N., Vogt, J.,  
643 and Suppan, P.: Evaluation of continuous ceilometer-based mixing layer heights and correlations  
644 with PM<sub>2.5</sub> concentrations in Beijing, in: *Remote Sensing of Clouds and the Atmosphere Xiv*, edited  
645 by: Picard, R. H., Schafer, K., Comeron, A., Kassianov, E., and Mertens, C. J., *Proceedings of SPIE*,  
646 2009.
- 647 Silvanus, P. T. F. R. S., and Gardner, M.: A Little More about Curvature of Curves, *Calculus Made*  
648 *Easy*, 249-262, [https://doi.org/10.1007/978-1-349-15058-8\\_25](https://doi.org/10.1007/978-1-349-15058-8_25), 1998.
- 649 Stone, R. S., Anderson, G. P., Shettle, E. P., Andrews, E., Loukachine, K., Dutton, E. G., Schaaf, C.,  
650 and Roman, M. O., III: Radiative impact of boreal smoke in the Arctic: Observed and modeled, *J.*  
651 *Geophys. Res.: Atmos.*, 113, <https://doi.org/10.1029/2007jd009657>, 2008.
- 652 Stull, R. B.: *An Introduction to Boundary Layer Meteorology*, 1988.
- 653 Su, T., Li, Z., and Kahn, R.: Relationships between the planetary boundary layer height and surface  
654 pollutants derived from lidar observations over China: regional pattern and influencing factors,  
655 *Atmos. Chem. Phys.*, 18, 15921-15935, <https://doi.org/10.5194/acp-18-15921-2018>, 2018.
- 656 Tang, G., Zhu, X., Hu, B., Xin, J., Wang, L., Munkel, C., Mao, G., and Wang, Y.: Impact of emission  
657 controls on air quality in Beijing during APEC 2014: lidar ceilometer observations, *Atmos. Chem.*  
658 *Phys.*, 15, 12667–12680, <https://doi.org/10.5194/acp-15-12667-2015>, 2015.



- 659 Tang, G., Zhang, J., Zhu, X., Song, T., Muenkel, C., Hu, B., Schaefer, K., Liu, Z., Zhang, J., Wang,  
660 L., Xin, J., Suppan, P., and Wang, Y.: Mixing layer height and its implications for air pollution over  
661 Beijing, China, *Atmos. Chem. Phys.*, 16, 2459-2475, <https://doi.org/10.5194/acp-16-2459-2016>,  
662 2016.
- 663 Tie, X., Huang, R.-J., Cao, J., Zhang, Q., Cheng, Y., Su, H., Chang, D., Poeschl, U., Hoffmann, T.,  
664 Dusek, U., Li, G., Worsnop, D. R., and O'Dowd, C. D.: Severe Pollution in China Amplified by  
665 Atmospheric Moisture, *Sci Rep*, 7, <https://doi.org/10.1038/s41598-017-15909-1>, 2017.
- 666 Wang, J. Z., Gong, S. L., Zhang, X. Y., Yang, Y. Q., Hou, Q., Zhou, C. H., and Wang, Y. Q.: A  
667 Parameterized Method for Air-Quality Diagnosis and Its Applications, *Adv. Meteorol.*,  
668 <https://doi.org/10.1155/2012/238589>, 2012.
- 669 Wang, L., Liu, J., Gao, Z., Li, Y., Huang, M., Fan, S., Zhang, X., Yang, Y., Miao, S., Zou, H., Sun,  
670 Y., Chen, Y., and Yang, T.: Vertical observations of the atmospheric boundary layer structure over  
671 Beijing urban area during air pollution episodes, *Atmos. Chem. Phys.*, 19, 6949-6967,  
672 <https://doi.org/10.5194/acp-19-6949-2019>, 2019.
- 673 Wang, X., Wei, W., Cheng, S., Li, J., Zhang, H., and Lv, Z.: Characteristics and classification of PM  
674 2.5 pollution episodes in Beijing from 2013 to 2015, *Sci. Total Environ.*, 612, 170-179,  
675 <https://doi.org/10.1016/j.scitotenv.2017.08.206>, 2018.
- 676 Wang, Y., Yao, L., Wang, L., Liu, Z., Ji, D., Tang, G., Zhang, J., Sun, Y., Hu, B., and Xin, J.:  
677 Mechanism for the formation of the January 2013 heavy haze pollution episode over central and  
678 eastern China, *Sci. China-Earth Sci.*, 57, 14-25, <https://doi.org/10.1007/s11430-013-4773-4>, 2014.
- 679 Wilcox, E. M., Thomas, R. M., Praveen, P. S., Pistone, K., Bender, F. A. M., and Ramanathan, V.:  
680 Black carbon solar absorption suppresses turbulence in the atmospheric boundary layer, *Proc. Natl.*  
681 *Acad. Sci. U. S. A.*, 113, 11794-11799, <https://doi.org/10.1073/pnas.1525746113>, 2016.
- 682 Xin, J., Gong, C., Wang, S., and Wang, Y.: Aerosol direct radiative forcing in desert and semi-desert  
683 regions of northwestern China, *Atmos. Res.*, 171, 56-65,  
684 <https://doi.org/10.1016/j.atmosres.2015.12.004>, 2016.
- 685 Xu, T., Song, Y., Liu, M., Cai, X., Zhang, H., Guo, J., and Zhu, T.: Temperature inversions in severe  
686 polluted days derived from radiosonde data in North China from 2011 to 2016, *Sci. Total Environ.*,  
687 647, 1011-1020, <https://doi.org/10.1016/j.scitotenv.2018.08.088>, 2019.



- 688 Yang, Y., Liao, H., and Lou, S.: Increase in winter haze over eastern China in recent decades: Roles  
689 of variations in meteorological parameters and anthropogenic emissions, *J. Geophys. Res.: Atmos.*,  
690 121, 13050-13065, <https://doi.org/10.1002/2016jd025136>, 2016.
- 691 Zhang, Q., Ma, Q., Zhao, B., Liu, X., Wang, Y., Jia, B., and Zhang, X.: Winter haze over North  
692 China Plain from 2009 to 2016: Influence of emission and meteorology, *Environ. Pollut.*, 242, 1308-  
693 1318, <https://doi.org/10.1016/j.envpol.2018.08.019>, 2018.
- 694 Zhang, R., Khalizov, A. F., Pagels, J., Zhang, D., Xue, H., and McMurry, P. H.: Variability in  
695 morphology, hygroscopicity, and optical properties of soot aerosols during atmospheric processing,  
696 *Proc. Natl. Acad. Sci. U. S. A.*, 105, 10291-10296, <https://doi.org/10.1073/pnas.0804860105>, 2008.
- 697 Zhang, Z., Zhang, X., Zhang, Y., Wang, Y., Zhou, H., Shen, X., Che, H., Sun, J., and Zhang, L.:  
698 Characteristics of chemical composition and role of meteorological factors during heavy aerosol  
699 pollution episodes in northern Beijing area in autumn and winter of 2015, *Tellus Series B-Chemical  
700 and Physical Meteorology*, 69, <https://doi.org/10.1080/16000889.2017.1347484>, 2017.
- 701 Zhao, D., Xin, J., Gong, C., Quan, J., Liu, G., Zhao, W., Wang, Y., Liu, Z., and Song, T.: The  
702 formation mechanism of air pollution episodes in Beijing city: Insights into the measured feedback  
703 between aerosol radiative forcing and the atmospheric boundary layer stability, *Sci. Total Environ.*,  
704 692, 371-381, <https://doi.org/10.1016/j.scitotenv.2019.07.255>, 2019.
- 705 Zheng, C., Zhao, C., Zhu, Y., Wang, Y., Shi, X., Wu, X., Chen, T., Wu, F., and Qiu, Y.: Analysis of  
706 influential factors for the relationship between PM<sub>2.5</sub> and AOD in Beijing, *Atmos. Chem. Phys.*,  
707 17, 13473-13489, <https://doi.org/10.5194/acp-17-13473-2017>, 2017.
- 708 Zheng, G. J., Duan, F. K., Su, H., Ma, Y. L., Cheng, Y., Zheng, B., Zhang, Q., Huang, T., Kimoto,  
709 T., Chang, D., Poeschl, U., Cheng, Y. F., and He, K. B.: Exploring the severe winter haze in Beijing:  
710 the impact of synoptic weather, regional transport and heterogeneous reactions, *Atmos. Chem. Phys.*,  
711 15, 2969-2983, <https://doi.org/10.5194/acp-15-2969-2015>, 2015.
- 712 Zhong, J., Zhang, X., Wang, Y., Sun, J., Zhang, Y., Wang, J., Tan, K., Shen, X., Che, H., Zhang, L.,  
713 Zhang, Z., Qi, X., Zhao, H., Ren, S., and Li, Y.: Relative Contributions of Boundary-Layer  
714 Meteorological Factors to the Explosive Growth of PM<sub>2.5</sub> during the Red-Alert Heavy Pollution  
715 Episodes in Beijing in December 2016, *J. Meteorol. Res.*, 31, 809-819,  
716 <https://doi.org/10.1007/s13351-017-7088-0>, 2017.



- 717 Zhong, J., Zhang, X., Wang, Y., Liu, C., and Dong, Y.: Heavy aerosol pollution episodes in winter  
718 Beijing enhanced by radiative cooling effects of aerosols, *Atmos. Res.*, 209, 59-64,  
719 <https://doi.org/10.1016/j.atmosres.2018.03.011>, 2018.
- 720 Zhu, X., Tang, G., Lv, F., Hu, B., Cheng, M., Muenkel, C., Schafer, K., Xin, J., An, X., Wang, G.,  
721 Li, X., and Wang, Y.: The spatial representativeness of mixing layer height observations in the North  
722 China Plain, *Atmos. Res.*, 209, 204-211, <https://doi.org/10.1016/j.atmosres.2018.03.019>, 2018.